Author(s): Komulainen, Sanna; Iresh Fernando, P. U. Ashvin; Mareš, Jiří; Selent, Anne; Khalili, Roya; Cesana, Paul T.; Ebeling, Andreas; Kantola, Anu M.; Beyeh, Ngong Kodiah; Rissanen, Kari; DeBoef, Brenton; Lantto, Perttu; Telkki, Ville-Veikko

Title: Encapsulation of xenon by bridged resorcinarene cages with high 129Xe NMR chemical shift and efficient exchange dynamics

Year: 2023

Version: Published version

Please cite the original version:

Komulainen, S., Iresh Fernando, P. U. A., Mareš, J., Selent, A., Khalili, R., Cesana, P. T., Ebeling, A., Kantola, A. M., Beyeh, N. K., Rissanen, K., DeBoef, B., Lantto, P., & Telkki, V.-V. (2023). Encapsulation of xenon by bridged resorcinarene cages with high 129Xe NMR chemical shift and efficient exchange dynamics. Cell Reports Physical Science, 4(2), Article 101281. https://doi.org/10.1016/j.xcrp.2023.101281

Cell Reports
Physical Science

CellPress
OPEN ACCESS

Article

Encapsulation of xenon by bridged resorcinarene cages with high ^{129}Xe NMR chemical shift and efficient exchange dynamics

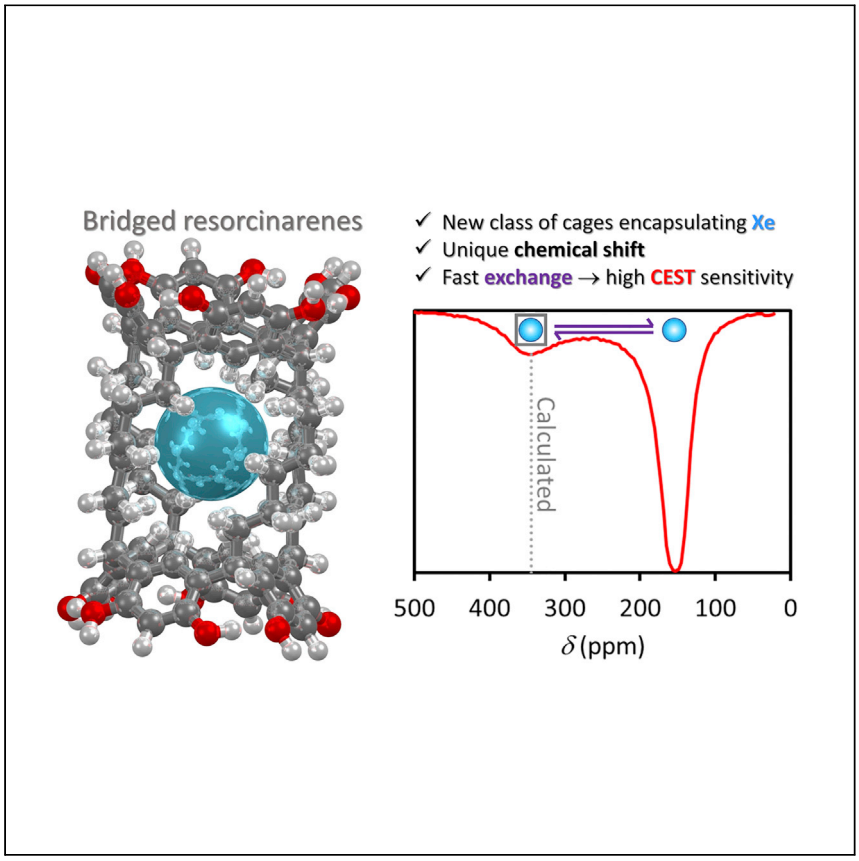

Xenon biosensors enable highly sensitive background-free molecular imaging. Komulainen et al. report a class of cages based on bridged resorcinarenes that encapsulate Xe; the high ^{129}Xe chemical shift provides contrast, while fast exchange dynamics offer CEST NMR sensitivity enhancement.

Sanna Komulainen, P. U. Ashvin Iresh Fernando, Jiří Mareš, ..., Brenton DeBoef, Perttu Lantto, Ville-Veikko Telkki

perttu.lantto@oulu.fi (P.L.)
ville-veikko.telkki@oulu.fi (V.-V.T.)

Highlights

Cages based on bridged resorcinarenes encapsulate Xe in methanol

High ^{129}Xe chemical shift provides a useful contrast

Fast exchange dynamics offer CEST sensitivity enhancement

Water-soluble versions envisioned for potential Xe biosensor applications

Komulainen et al., Cell Reports Physical Science 4, 101281
February 15, 2023
https://doi.org/10.1016/j.xcrp.2023.101281

Cell Reports
Physical Science

CellPress
OPEN ACCESS

Article

Encapsulation of xenon by bridged resorcinarene cages with high ^{129}Xe NMR chemical shift and efficient exchange dynamics

Sanna Komulainen,[1] P. U. Ashvin Iresh Fernando,[2] Jiří Mareš,[1] Anne Selent,[1] Roya Khalili,[1] Paul T. Cesana,[2] Andreas Ebeling,[1] Anu M. Kantola,[1] Ngong Kodiah Beyeh,[3] Kari Rissanen,[4] Brenton DeBoef,[2] Perttu Lantto,[1,*] and Ville-Veikko Telkki[1,5,*]

SUMMARY

Functionalized cages encapsulating xenon atoms enable highly sensitive, background-free molecular imaging through a technique known as HyperCEST ^{129}Xe MRI. Here, we introduce a class of potential biosensor cage structures based on two resorcinarene macrocycles bridged either by aliphatic carbon chains or piperazines. First-principles-based modeling predicts a high chemical shift (about 345 ppm) outside the typical experimental observation window for ^{129}Xe encapsulated by the aliphatically bridged cage and two ^{129}Xe resonances for the piperazine-bridged cages corresponding to single and double loading. Based on the computational predictions as well as ^{129}Xe chemical exchange saturation transfer (CEST) and T_2 relaxation nuclear magnetic resonance experiments, we confirm Xe encapsulation in the aliphatically bridged and double encapsulation in the piperazine-bridged resorcinarene in methanol. The cages show fast Xe exchange rates (12,000–49,000 s^{-1}), resulting in a high CEST response regardless of the relatively low binding constant (0.09–3 M^{-1}).

INTRODUCTION

Xenon biosensors offer a means for sensitive and background-free molecular imaging.[1–4] The biosensors include functionalized cages encapsulating Xe atoms. The spatial distribution of the biosensors in living systems is monitored by ^{129}Xe MRI. ^{129}Xe chemical shift is very sensitive to changes in the local physical and chemical environment of Xe, providing information about Xe encapsulation and biosensor binding. MRI sensitivity of ^{129}Xe can be improved up to seven orders of magnitude by combining spin-exchange optical pumping (SEOP) nuclear hyperpolarization method[5] with chemical exchange saturation transfer (CEST) technique.[6] Therefore, Xe biosensors allow molecular imaging even at nano- or picomolar concentrations. For example, the method has been exploited in cell tracing,[7] biothiol detection,[8] and *in vivo* bioimaging of living rats.[9]

The sensitivity and specificity of the Xe biosensor is strongly affected by the properties of the cages encapsulating Xe atoms.[4] For example, the cages should have a high enough affinity toward Xe so that the encapsulation takes place; the encapsulated ^{129}Xe should provide a signal at chemical shift distinct from solvent and other signals; the exchange rate of Xe between encapsulated and solvent pools should be high enough for efficient CEST but slow enough for resolving the sites in the nuclear

[1]NMR Research Unit, University of Oulu, 90570 Oulu, Finland

[2]Department of Chemistry, University of Rhode Island, Kingston, RI 02881, USA

[3]Department of Chemistry, Oakland University, 146 Library Drive, Rochester, MI 48309-4479, USA

[4]Department of Chemistry, University of Jyvaskyla, 40014 Jyväskylä, Finland

[5]Lead contact

*Correspondence: perttu.lantto@oulu.fi (P.L.), ville-veikko.telkki@oulu.fi (V.-V.T.)

https://doi.org/10.1016/j.xcrp.2023.101281

magnetic resonance (NMR) timescale; and the cage should be functionalizable for targeting a desired biological target.

Cryptophane cages are considered as the gold standard for Xe biosensor applications as they exhibit the highest Xe binding constant.[2] However, they are not commercially available, their synthesis requires multiple steps, and yields are very low.[2] Therefore, alternative biosensor cage structures are actively screened to overcome these drawbacks. One commonly used cage structure is cucurbit[6]uril (CB6), which is a commercially available macrocyclic host.[10] It suffers from limited solubility and promiscuous molecular recognition behavior where Xe is easily replaced by other guests, and post-functionalization of CB6 is very challenging.[11] Variable other macrocycle and cage compounds have also been introduced as potential candidates, such as cucurbituril-based rotaxanes,[12] pillararenes,[13,14] hemicarcerands,[15] Fe_4L_6 cages,[16,17] cyclodextrins,[18,19] calixarenes,[20] and chiral bisurea-bisthiourea macrocycles.[21] In some works cryptophanes have been linked together to increase sensitivity.[22–24] The payload of Xe has also been increased by so-called super hosts, including gas vesicles,[25] nanoemulsions,[26] bacteriophages,[27] nanodroplets,[28] genetically encoded proteins,[29] and functionalized liposomes and micelles.[30,31] The cage molecule can also be associated with a lipid layer, which aids in transportation into the body.[32,33] The strengths and weaknesses of each Xe biosensor host type are evaluated thoroughly in the recent review by Jayapaul and Schröder.[2]

Here, we introduce a class of potential biosensor cage structures based on two resorcinarene supramolecules bridged either by aliphatic carbon chains or piperazines. Resorcinarene is a calixarene-type macrocycle formed by a simple synthesis.[34] Mannich condensation is a common procedure to modify the aromatic ring structure and form cage structures by connecting two resorcinarene structures with amine linkers.[35] By adjusting the linker structure, the properties of the cage can be easily modified, and different variations of cage structures can be synthesized. We report first principles computational predictions of chemical shifts of ^{129}Xe atoms in both aliphatically bridged and piperazine-bridged resorcinarenes. The modeling provides the direct ^{129}Xe chemical shift information with microscopic interpretation, which has earlier revealed beneficial details about the encapsulation of Xe in cryptophanes,[36,37] Fe_4L_6 cages,[16,17] Buckminster fullerene,[38–40] clathrates,[41] zeolites,[42,43] metal organic frameworks,[44,45] porous organic cages,[46,47] liquid crystals,[48] and water.[49] Encapsulation of Xe in the cages in methanol solvent is confirmed by experimental ^{129}Xe CEST and T_2 relaxation analysis. Furthermore, simulations of CEST spectra reveal essential exchange rates and binding constants.

RESULTS AND DISCUSSION

Computational modeling predicts xenon encapsulation and ^{129}Xe chemical shifts

The computationally modeled structures of the aliphatically bridged and piperazine-bridged resorcinarene cages ABR-6 and PBR-3 are illustrated in Figures 1A and 1B, respectively. In the computational modeling, the structures of the cages were optimized with a xenon atom inside the cages, also considering the effect of methanol solvent (see computational section in experimental procedures). The PBR-2 cage is otherwise like the PBR-3 cage, but the lengths of the carbon chains pointing outward from the resorcinarenes are two instead of three.

The volume of the optimized ABR-6 cage cavity was relatively small, only 52 Å^3, compared with the van der Waals volume of Xe, 42 Å^3. The ratio of the guest/host volumes is 0.81, which is larger than the optimal ratio of 0.55 $\pm$ 0.09 for

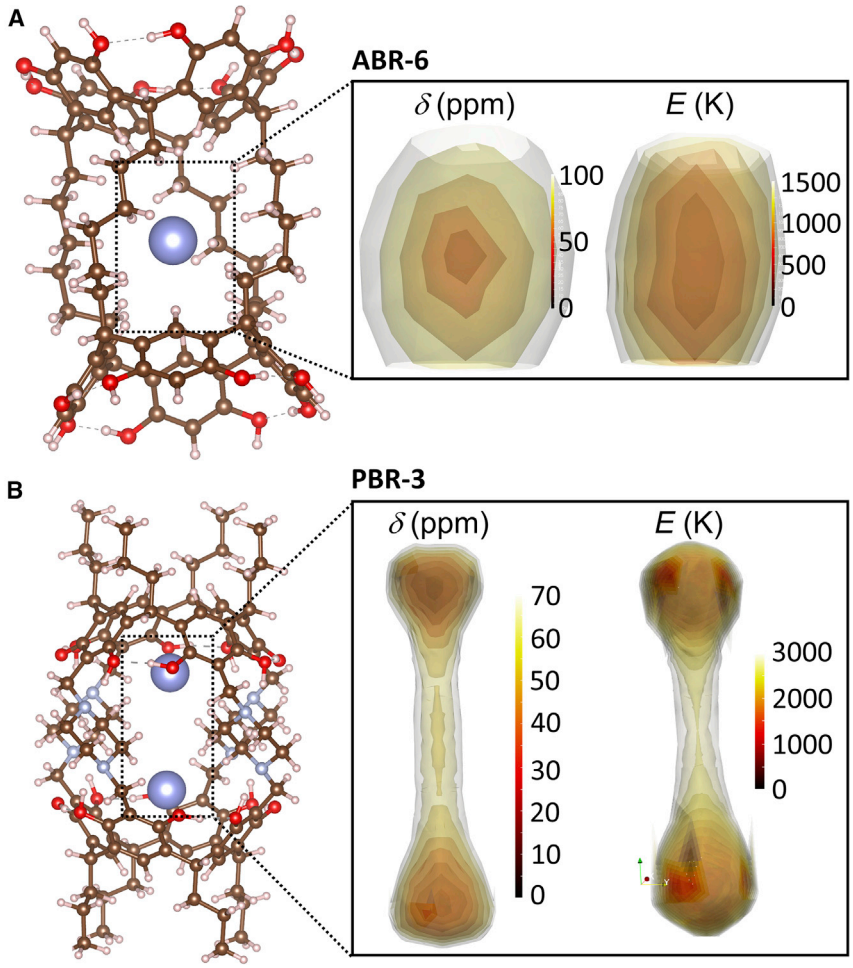

Figure 1. Computational modeling of xenon in resorcinarene cages

Structures of (A) the aliphatically bridged (ABR-6) and (B) piperazine-bridged (PBR-3) resorcinarene cages. Carbon, oxygen, nitrogen, and hydrogen atoms are illustrated by brown, red, blue, and white colors, respectively. The large blue ball represents an encapsulated xenon atom. Examples of ^{129}Xe chemical shift (δ) and potential energy (E) surfaces with respect to the equilibrium values of the encapsulated xenon are shown on the right.

encapsulation.[50] The ABR-6 cavity volume is also smaller than that of cryptophane-A (87–119 Å^3)[51,52] and cryptophane-1.1.1 (81 Å^3).[53]

The PBR-2 and PBR-3 cages include a long, hourglass-shaped cavity (Figure 1B), in which xenon atoms have two potential binding sites at each end of the cavity. The overall volume of the cavity is 163 Å^3. Therefore, the volume of one binding site is about 81 Å^3, and the guest/host volume ratio is 0.52, which is close to the optimal ratio. The simulations imply that the PBR cages could potentially encapsulate two xenon atoms simultaneously.

The nudged elastic band (NEB) simulations[54,55] show that the potential energy of xenon atom entering or exiting the ABR or PBR cages is smaller when the path goes through the sides of the cages (horizontal direction in Figure 1) instead of the ends (vertical direction). The exit potential energy barrier is about three times higher through the end than through the side (ABR-6: 246 vs. 59 kJ/mol, PBR-3: 250 vs. 88 kJ/mol). The potential energies for PBR-2 are almost identical to PBR-3.

This implies that the sides are the predominant entrances for xenon encapsulation, which is reasonable considering the flexible nature of the aliphatic and piperazine chains bridging the resorcinarenes. On the other hand, the NEB simulations do not consider the entropic contributions.

We calculated the ^{129}Xe chemical shifts of xenon inside the cages at equilibrium geometry using the density functional theory (DFT) method, including both scalar relativistic (SR) and spin-orbit (SO) relativistic effects (see "X2C + SO" results in Table S5). Furthermore, we took the temperature-dependent motion of a xenon atom inside the cavity into account by MC averaging over potential energy and ^{129}Xe chemical shift surfaces (Figure 1, Tables S6 and S7) computed at SR level (the cage mobility was not considered).

The averaged computational ^{129}Xe chemical shift of xenon in ABR-6 is 345 ppm at 300 K. The shift is much higher than typical shifts in cryptophanes (30–70 ppm),[2] and it is even higher than the extraordinarily high chemical shift of a permetallated cryptophane cage (308 ppm).[56] The high chemical shift is a consequence of the small size of the ABR-6 cavity; chemical shift of Xe is known to increase with decreasing pore/cavity size.[57] We note that, contrary to the permetallated cryptophane cage,[56] ABR-6 does not include metal ions. Therefore, instead of metal effect,[37] the large Xe shift in ABR-6 is due to high density of virtual electronic states provided by neighboring cage atoms, which are available for the paramagnetic deshielding contribution.[58] The shift is outside the typical experimental observation window, and the computational predictions guided us to the appropriate chemical shift range in the CEST experiments.

The calculated chemical shift of a single xenon atom inside the PBR-3 is 109 ppm at 300 K, which is also slightly higher than the typical shift in cryptophanes, once again due to the slightly smaller volume of the binding site within the PBR-3 cage. When the cage includes two xenon atoms, the calculated shift increases ca. 45 ppm due to Xe-Xe interactions (Table S8), being 154 ppm. Consequently, the simulations predict that one might observe two bound xenon signals from the PBR-3 cages. The calculated chemical shift of a single xenon in the PBR-2 cage is 7 ppm smaller than in the PBR-3 cage.

^{129}Xe NMR measurements show xenon encapsulation and exchange dynamics

Direct thermally polarized ^{129}Xe spectra of all the three cages include only a single, relatively narrow peak at around 142 ppm at 300 K, originating from ^{129}Xe in the methanol solvent (Figure 2). The concentration of Xe in methanol, which was calculated to be about 350 mM at 4 atm pressure using the Ostwald coefficient $L = 2.09$,[59] is 350 and 175 times higher than the concentrations of the ABR-6 and PBR cages (1 and 2 mM), respectively. Therefore, the signal of ^{129}Xe in the cages is hundreds of times smaller than the solvated ^{129}Xe signal, vanishing to the noise.

However, thermally polarized ^{129}Xe CEST spectra include additional peaks, which reveal that some of the cages encapsulate xenon. The bound xenon signals become visible due to the significant sensitivity enhancement (three to four orders of magnitude) provided by CEST.[2]

The CEST spectra of ABR-6 include a broad and low dip of encapsulated ^{129}Xe above 300 ppm. The spectra were simulated using a two-site (solvent and cage sites) exchange model and Bloch-McConnell equations (dotted lines in Figure 2). The CEST simulations were not performed to ABR-6 data at 300 K because of the very

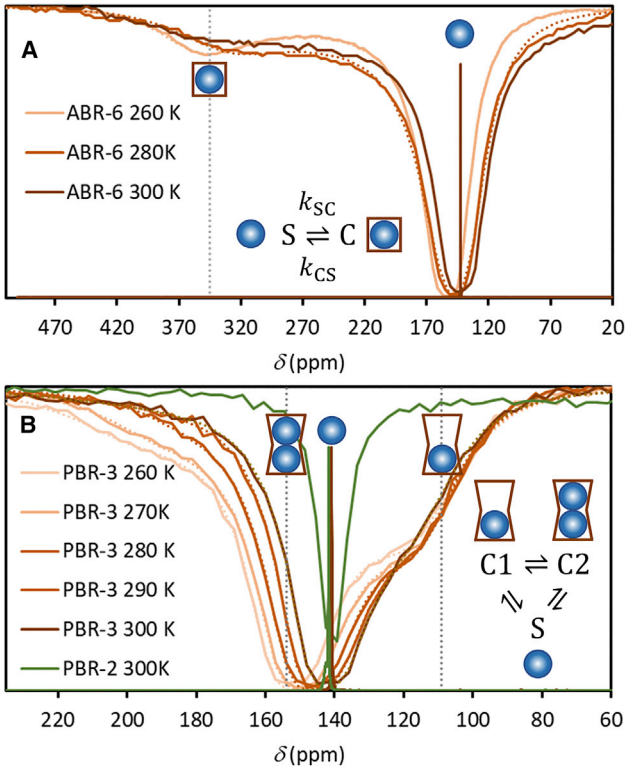

Figure 2. Detection of encapsulation of xenon in resorcinarene cages

^{129}Xe direct (peaks up) and CEST (peaks down) NMR spectra of xenon in (A) ABR-6 as well as (B) PBR-2 and PBR-3 cages in methanol. Simulated CEST spectra are illustrated by dotted lines. Calculated shifts of ^{129}Xe in cages are shown by gray vertical dotted lines. The figures also visualize the two- and three-site exchange models that were used in the simulations. S and C refer to the solvent and cage sites, respectively. C1 and C2 refer to the PBR-3 cages filled with one and two Xe atoms, respectively. The CEST saturation pulse length and B_1 field strength for the ABR-6 sample were 1 s and 39 μT. The corresponding values for the PBR samples were 5 s and 59 μT.

broad signal due to fast exchange. According to the simulations, the chemical shift of ^{129}Xe in the ABR-6 cage is 340 ± 4 ppm at 280 K (Figure 3A), which is in excellent agreement with the shift predicted by the DFT calculations (345 ppm at 300 K). The exchange rate k_{CS} is very high, 52,000 ± 3,000 s^{-1} at 280 K (Figure 3B). It is much higher than k_{CS} for commonly used cryptophane-A-monoacid (CrA) cage in DMSO, 317 s^{-1},[60] and even higher than for CB6 (1,470 s^{-1} in PBS buffer), which has an open ring structure.[10] The relative population of the cage site (i.e., the relative amount of bound Xe) is low, 0.00150 ± 0.00014 at 280 K (Figure 3C), predominately due to the much lower cage concentration than Xe concentration. About 52% of cages are occupied by Xe at 280 K. Xe binding constant is rather low, 3.1 ± 0.7 M^{-1} at 280 K (Figure 3D), compared with the typical range of different cryptophane cages, 5–3,000 M^{-1}[61,62]; increasing water solubility with polar groups makes binding constants even larger,[2] and the water-soluble versions of CrA have binding constants up to 30,000 M^{-1}.[56,63,64] On the other hand, the ABR-6 Xe binding constant is similar to many other novel alternative biosensor candidates, such as gas binding proteins (40 M^{-1}),[2] Fe-MOP (16 M^{-1}),[16] α-cyclodextrin (20 M^{-1}),[65] and calix[4]arene derivative (14 M^{-1}).[20]

The CEST response of the PBR-3 sample includes strong asymmetric broadening toward lower chemical shifts, which indicates the Xe encapsulation. Furthermore, there

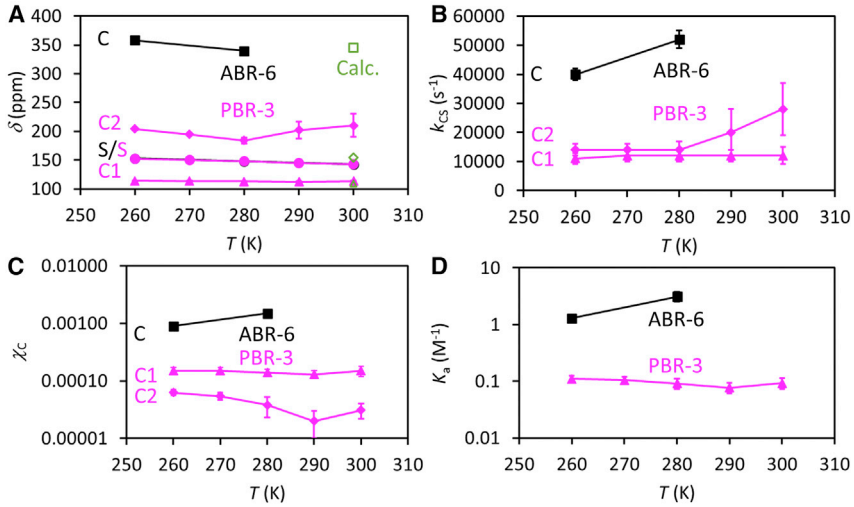

Figure 3. Chemical and thermodynamic parameters for xenon encapsulation

Parameters resulting from the simulations of ^{129}Xe CEST spectra of the ABR-6 and PBR-3 samples.

(A) Chemical shifts.

(B) Exchange rates.

(C) Relative populations of the cage sites.

(D) Binding constants.

The error margins show the 95% confidence interval given by the Bayesian posterior distribution obtained by the MCMC simulation.

is weak broadening toward high chemical shifts as well, especially at the lowest temperatures. This may be an indication of simultaneous encapsulation of two Xe atoms in the hourglass-shaped cage. Therefore, in the CEST spectra simulations, we used a three-site exchange model instead of two. As visualized in Figure 2B, the sites include the solvent pool (S) and two cage pools corresponding to single (C1) and double (C2) Xe loading. An interesting detail in the model is that when one Xe is released from the C2 pool to solvent, simultaneously the remaining Xe changes from C2 to C1 pool without any physical exchange. According to the CEST simulations, chemical shift of a single ^{129}Xe in the PBR-3 cage is 114 $\pm$ 1 ppm (Figure 3A), being close to the shift predicted by the DFT calculations (109 ppm). The shift of the double-loaded cage is higher with a value of 210 $\pm$ 20 ppm at 300 K, which is in qualitative agreement (right direction) with the DFT prediction (154 ppm). Probably both simple droplet model as well as entailing approximations by semi-empirical theory in molecular dynamics (MD) simulations cause the underestimation of the chemical shift due to double occupation. The single-loading exchange rate k_{C1S} is high, 12,000 $\pm$ 3,000 s^{-1} at 300 K (Figure 3B), but about four times smaller than for ABR-6 cage. The double-loading exchange rate (28,000 $\pm$ 9,000 s^{-1} at 300 K) is even higher because there are two Xe atoms that can exit instead of one. The relative populations of the cage sites C1 and C2, 0.00015 $\pm$ 0.00003 and 0.000031 $\pm$ 0.000009 at 300 K (Figure 3C), are about ten times smaller than in the ABR-6 cage, although the concentration of PBR-3 cages is two times higher. Only about 3% of the cages are occupied by Xe. Xe binding constant in PBR-3 is low, 0.09 $\pm$ 0.02 M^{-1}, about 30 times smaller than in ABR-6.

The ^{129}Xe CEST spectrum of PBR-2 cage includes only a symmetric solvent resonance, without any sign of encapsulated Xe signal. According to the DFT predictions, the signal of a single encapsulated Xe has about 7 ppm smaller chemical shift than in PBR-3 cage, which should be well resolved in the spectrum without disruptive

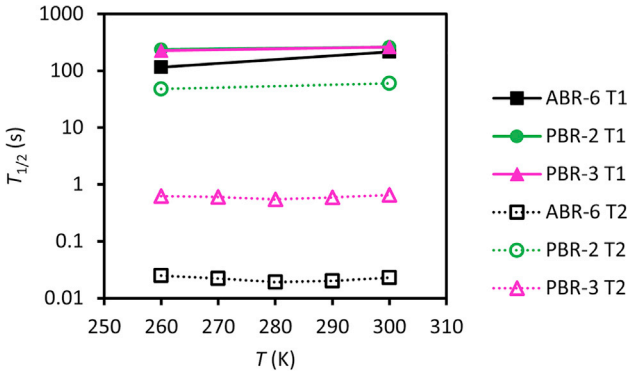

Figure 4. Relaxation times reflecting the exchange dynamics of xenon
T_1 and T_2 relaxation times of ^{129}Xe in the ABR-6, PBR-2, and PBR-3 samples.

overlapping with the solvent signal. Therefore, the CEST experiments imply that, contrary to PBR-3, the PBR-2 cage does not encapsulate Xe, regardless of the very similar structure of the cages. We expect that this is a consequence of the fact that all the residual solvent from synthesis and purification was removed in PBR-3, but PBR-2 still had some tightly encapsulated alcoholic (ethanol and methanol) solvents. It is likely that the entrapped solvent prevents the encapsulation of Xe in PBR-2.[35]

Relaxation measurements provide alternative contrast for xenon encapsulation and exchange dynamics

Relaxation measurements offer an alternative perspective on Xe dynamics in the samples. T_1 relaxation times of ^{129}Xe in the PBR-2 and PBR-3 samples are long and almost equal, 260 and 263 s at 300 K, respectively (Figure 4). Providing that PBR-3 cages encapsulate Xe but PBR-2 cages do not, it seems that T_1 is not sensitive to exchange, which is reasonable, as the exchange rate (~10 kHz) is much lower than the Larmor frequency (166 MHz).[66] T_1 in the ABR-6 sample is slightly lower, 214 s at 300 K, because it was measured at a lower field (138 MHz).[66]

T_2 of ^{129}Xe in the PBR-2 sample (60 s at 300 K) is much longer than that in the ABR-6 and PBR-3 samples (23 and 650 ms, respectively). T_2 of ^{129}Xe is known to be very sensitive to chemical exchange,[46,47] and the long T_2 provides an additional confirmation that PBR-2 does not encapsulate Xe, while the short T_2 affirms Xe binding in PBR-3 and ABR-6 cages.

According to a simple two-site exchange model, in which T_2 relaxation is assumed to arise from varying chemical shift due to exchange between two sites, T_2 relaxation rate $R_2 = 1/T_2$ is[67,68]

$$R_2 = \frac{\chi_S \chi_C \Delta\omega^2 k}{(\chi_S k)^2 + \Delta\omega^2}, \qquad \text{(Equation 1)}$$

where χ_S and χ_C are the relative populations of Xe in the solvent and cage sites, $\Delta\omega = \omega_C - \omega_S$ is the ^{129}Xe angular frequency difference between the cage and solvent sites, and $k = k_{SC} + k_{CS}$ is the exchange rate. Here, the relaxation rate is independent of the CPMG echo time, as the inverse of the exchange rate (0.02–0.1 ms) is much shorter than the echo time (1 ms); hence, relaxation dispersion can be neglected, and T_2 relaxation-based exchange analysis is significantly simplified, as pointed out earlier by Kunth et al.[68]

Using the parameters given by the CEST simulations (Figure 3), Equation 1 predicts that T_2 values of the ABR-6 and PBR-3 samples are 14 $\pm$ 4 ms at 280 K and 600 $\pm$ 300 ms at 300 K, respectively, which are in good agreement with the corresponding experimental T_2 values, 19 and 652 ms. Therefore, the model provides a reasonable explanation for the shorter T_2 of the ABR-6 sample, which predominantly originates from a larger chemical shift difference between the cage and solvent sites than in the PBR-3 sample. Furthermore, it confirms that the parameter values resulting from the CEST simulations are reliable. Overall, the relaxation experiments show that T_2 offers extremely sensitive contrast for Xe binding; T_2 of PBR-3 sample was about 90 times shorter than that of PBR-2 due to the encapsulation. This contrast could be exploited in the biosensor studies instead of CEST contrast because T_2 can be measured very efficiently even in a single scan by the CPMG (Carr-Purcell-Meiboom-Gill) method. This was demonstrated earlier by Kunth et al. for Xe encapsulated by cryptophane-A monoacid (CrA-ma) and CB6 cages.[68] As pointed out by Kunth et al., relaxation rate is approximately linearly dependent on the concentration of cages, and exchange-induced relaxivity $r_2 = \Delta R_2/\Delta C$ (where ΔR_2 and ΔC are the changes in relaxation rate and cage concentration, respectively) is a useful parameter to compare T_2 relaxation contrasts of the cages for Xe encapsulation. ABR-6 has much higher relaxivity (r_2 = 53 s^{-1} mM^{-1}) than PBR-3 (r_2 = 0.83 s^{-1} mM^{-1}); it is higher than relaxivity of CrA-ma (r_2 = 13 s^{-1} mM^{-1}) but lower than that of CB6 (r_2 = 870 s^{-1} mM^{-1}).[68] Naturally, in the biosensor applications the contrast is diminished due to Xe interactions with proteins and other constituents of the sample, but even in those conditions, detectable contrast remains.[69]

Envisioning ways to make cages water soluble

The ABR-6 and PBR cages studied in this work were dissolved in methanol. In biosensor applications, the water solubility of xenon binding cages is essential for *in vivo* studies. Hence, we propose several potential synthetic directions toward enhancing the water solubility of ABR-6 cage structure without affecting the hydrophobic cavity of the cage. It has been reported that the addition of anions and cations enabled the organic soluble pillar[n]arenes and resorcinarenes to be water soluble.[14,70–72] Utilizing similar principles, ABR-6 can be functionalized with these charged moieties to increase the water solubility, as illustrated in Figures S1A and S1B. Two alternative routes are represented in Figures S1C and S1D.[70,71] Although these modifications as well as the change of solvent affect the structure of the cages, we anticipate that the structural changes are not significant, and therefore the bound Xe chemical shifts are expected to be close to those in unmodified cages in methanol solvent. On the other hand, chemical shift of free Xe in solvent increases about 48 ppm when solvent is changed from methanol to water.[73] Therefore, the chemical shift difference between the solvent and dominant single-loading cage sites is expected to increase in PBR-3 cage in water, improving resolution. In ABR-6, the difference is expected to decrease, but, due to the exceptionally high chemical shift of bound Xe in ABR-6 (about 340 ppm), the effect of the decreased difference on resolution is assumed to be insignificant.

In conclusion, we introduced a class of cages based on two resorcinarene macrocycles bridged by aliphatic carbon chains or piperazine, which can encapsulate Xe in methanol solvent and are therefore promising potential alternative cages for Xe biosensor applications, if they are modified water soluble as envisioned in the article. Thermally averaged first principles DFT calculations predicted an extraordinarily high chemical shift (345 ppm) of ^{129}Xe in the aliphatically bridged resorcinarene cage ABR-6. The shift is outside the typical range of ^{129}Xe resonances, thus providing unambiguous contrast for potential biosensor applications. Furthermore, the DFT calculations forecasted a signal of single encapsulated ^{129}Xe in the PBR

cages at around 110 ppm and another higher chemical shift signal from the cages loaded with two Xe atoms. Experimental thermally polarized ^{129}CEST spectra confirmed the encapsulation of Xe in ABR-6 and PBR-3 cages, and the observed ^{129}Xe chemical shifts of bound xenon were in excellent agreement with the DFT predictions. The binding constants of the ABR-6 and PBR-3 cages are modest, about 3 and 0.09 M^{-1}. However, the exchange rates are extraordinarily high, 52,000 and 12,000 s^{-1}, making the CEST response of the cages very strong because of high turnover, regardless of the low binding constant. This is promising for potential biosensor applications. We envision that the binding constant could be significantly increased by making the cages water soluble through the procedures described in the article.[56,63,64] Improved binding constant may be needed to avoid potential competing guests preventing Xe encapsulation.[74] Furthermore, changing methanol solvent to water may decrease saturation powers required in the CEST experiments if the relative size of bound Xe pool increases and exchange rate slightly reduces. The concentration of cages was rather high (1–2 mM) in the thermally polarized experiments reported in this article. However, the sensitivity of the CEST and relaxation experiments can be enhanced up to five orders of magnitude by SEOP hyperpolarization method,[5,6] potentially making sub-micromolar cage concentrations observable. Overall, the article clearly shows how combining state-of-the-art dynamical modeling of ^{129}Xe NMR chemical shift with modern experimental methods provides interesting and valuable information on Xe encapsulation in bridged resorcinarene cages, and it paves the way for finding affordable, readily synthesizable, efficient biosensor cages.

EXPERIMENTAL PROCEDURES

Resource availability

Lead contact

Further information and requests for resources should be directed to and will be fulfilled by the lead contact, Ville-Veikko Telkki (ville-veikko.telkki@oulu.fi).

Materials availability

All materials generated in this study are available from the lead contact without restriction.

Data and code availability

All data supporting the findings of this study are presented within the article and supplemental information. This study did not generate any datasets.

Bridged resorcinarene cages

We studied two piperazine and one aliphatically bridged resorcinarene cages. Their syntheses are described elsewhere.[35,75]

The chains bridging resorcinarenes in the ABR cage include six carbon atoms, and therefore the cage is called ABR-6. Contrary to the PBR cages, polar hydroxyl groups of resorcinarene cups point outward in the ABR cages (Figure 5A).[75] The two PBR cages are otherwise similar, but the length of carbon chains pointing outward from the resorcinarenes are two and three for the cages labeled PBR-2 and PBR-3, respectively (Figure 5B).

Sample preparation

Cage molecules were dissolved to MeOD-d_4, and the solution was transferred into 10-mm (ABR cages) or 5-mm (PBR cages) medium-wall NMR tubes. The concentrations of the ABR and PBR cages were 1 and 2 mM, respectively. Thereafter, the NMR

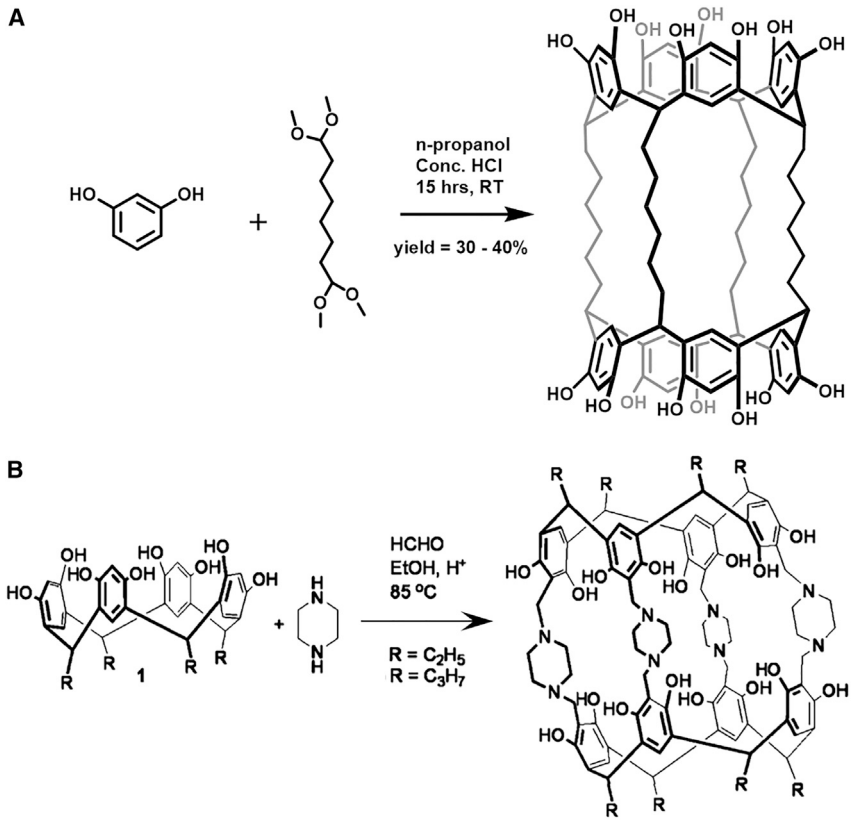

Figure 5. Synthesis of the resorcinarene cages

Synthetic schemes for the preparation of (A) ABR-6 as well as (B) PBR-2 (R = C_2H_5) and PBR-3 (R = C_3H_7) cages.[35,75]

tube was connected to a vacuum line, immersed in liquid nitrogen, and ^{129}Xe isotope-enriched (91%) xenon gas was condensed into the sample. The final xenon gas pressure in the samples was estimated to be about 3–4 atm.

^{129}Xe NMR measurements

Thermally polarized ^{129}Xe NMR experiments of the ABR-6 sample were carried out on a Bruker Avance III 500 spectrometer with a magnetic field of 11.75 T and ^{129}Xe frequency of 138 MHz using a 10-mm BBO probe with z-gradients. Thermally polarized ^{129}Xe NMR experiments of the PBR samples were measured on a Bruker Avance III 600 spectrometer with the magnetic field of 14.1 T and ^{129}Xe frequency of 166 MHz using a 5-mm BBFO probe with z-gradients. The temperature stabilization time was 60 min for the 10-mm and 30 min for the 5-mm samples in the variable temperature experiments.

^{129}Xe spectra were measured using a standard single-pulse program with a pulse angle of 15° for the 10-mm ABR-6 sample and 30° for the 5-mm PBR samples. The number of scans was 20,480 and 1,024, respectively. Recycling delay was adjusted according to the Ernst angle to maximize the signal-to-noise ratio per unit time: $0.0347 \times T_1$ in the case of the 15° pulse angle and $0.143 \times T_1$ in the case of the 30° pulse angle. Experiment times were 2 days and 11 h, respectively. The ^{129}Xe spectra and CEST spectra were referenced with respect to the signal of the 2 atm ^{129}Xe sample set at 0 ppm.

In the ^{129}Xe CEST NMR experiments of the 10-mm ABR-6 sample, the length and power of the continuous wave saturation pulse were 1 s and 200 mW (B_1 = 39 μT), respectively. Corresponding values for the 5-mm PBR samples were 5 s and 100 mW (B_1 = 59 μT). The number of accumulated scans was 8 and 2 for the ABR-6 and PBR samples, respectively. Recycling delay was adjusted according to Ernst's angle to be at least $1.257 \times T_1$, as the read pulse angle was 90°.

^{129}Xe T_1 and T_2 relaxation times were measured using standard inversion recovery and CPMG pulse sequences, respectively. In the CPMG experiments, the echo time was 1 ms, and eight time points were collected at appropriate echo numbers to observe T_2 decay.

CEST spectra simulations

The CEST simulations were done using the fast matrix-exponential method[76] for solving the Bloch-McConnell equations,[77] modified here to include a chemical exchange between small pools. The implementation was based on a previously published MATLAB code,[78] modified and rewritten to a Python language in this work. The fitting was facilitated by Markov chain Monte Carlo simulation[79] implemented in Håkansson et al.,[80] modified and rewritten into Python language in this work.

Computational section

The reference equilibrium structures of both piperazine-bridged (PBR-2 and PBR-3) as well as aliphatically bridged (ABR-6) resorcinarene cages were optimized with a Xe inside the cage using Turbomole code.[81,82] Optimizations were carried out with hybrid PBE0 functional[83] using D4 dispersion correction,[84] SR spin-free exact two-component (X2C) theory,[85] and x2c-TZVPall-s basis set for Xe[86] and def2-TZVP basis sets for cage atoms.[87] The effect of methanol solvent on the structure was accounted for by COSMO model.[88] The corresponding equilibrium structures for PBR-3 and ABR-6 are displayed in Figures 1A and 1B, respectively, and the XYZ-files of all three structures can be found in supplemental information. At the optimized equilibrium geometries, ^{129}Xe NMR nuclear shielding tensors were computed at the above-mentioned level of theory. In addition, the effect of non-relativistic theory as well as electron correlation treatment with pure Perdew-Burke-Ernzerhof (PBE)[89] and another hybrid Becke-half-and-half-Lee-Yang-Parr (BHandHLYP)[90,91] DFT functionals were tested. SO effect on ^{129}Xe NMR chemical shift was estimated by carrying out both scalar (SR-ZORA) and scalar plus spin-orbit (SO-ZORA) relativistic zeroth-order regular approximation calculations[92,93] with ADF code.[94,95] TZ2P-J basis set for Xe and DZP basis sets for cage atoms[96] together with a finite nuclear model[97] were used in ADF calculations.

We also computed potential energy and ^{129}Xe NMR shielding hypersurfaces at SR X2C level[98] in Turbomole code[81,82] inside *unrelaxed* PBR-3 and ABR-6 cages as well as *relaxed* ABR-6 cages (partially optimized cage geometries as Xe is displaced from the equilibrium position; see details in the supplemental information). In PBR-3, the performance of pure PBE functional was tested against benchmark[38–40] quality BHandHLYP functional. Produced potential energy surfaces and ^{129}Xe NMR shielding hypersurfaces were used in finite temperature canonical Monte Carlo (MC-NVT) simulation carried out with in-house MC-NVT code.[16] In the ABR-6 cage, the effect of the relaxation of the cage structure (*relaxed* structures) as Xe atom moves inside was tested at *first principles* DFT/PBE-D4 level as well as with extended tight-binding (xTB)[99] semi-empirical GFN1-xTB[100] and GFN2-xTB[101] methods.

MD simulations at T = 300 K of a finite droplet consisting of either one or two Xe atoms inside PBR-3 cage surrounded by explicit solvent of 300 methanol molecules were carried out with GFN1-xTB method in xTB code.[99] Xe NMR shielding averages were obtained by sampling snapshots from the MD trajectories. NMR calculations were carried out with Turbomole code at the same X2C/PBE/TZVP level (see above) for a cluster containing only Xe atom(s) and PBR-3 cage.

Cavity volumes of equilibrium structures were computed with Caver analyst code[51] using a probe radius of 1.2 Å with 10^5 samples.

To estimate the energy barrier associated with the Xe atom entering or leaving the cages, we used a zoom climbing image version of an NEB method implemented in ORCA 5.0.1.[54,55] Calculations at GFN1-xTB,[100] GFN2-xTB,[101] and B97-3c[102] levels were done both *in vacuo* and with analytical linearized Poisson-Boltzmann (ALPB)[103] and SMD[104] implicit solvation models for methanol. As for the conclusions of this study, neither the level of theory nor the implicit solvation model was significant. Therefore, the reported results were carried out at GFN2-xTB level of theory *in vacuo*.

SUPPLEMENTAL INFORMATION

Supplemental information can be found online at https://doi.org/10.1016/j.xcrp.2023.101281.

ACKNOWLEDGMENTS

Financial support from the European Research Council (Project number 772110), Academy of Finland (grant no. 340099), and the University of Oulu (Kvantum Institute) is gratefully acknowledged. Part of the work was carried out with the support of the Center for Material Analysis, University of Oulu, Finland. Computational resources of CSC (Espoo, Finland) and the Finnish Grid and Cloud Infrastructure project (persistent identifier urn:nbn:fi:research-infras-2016072533) were used. American Chemical Society (N.K.B.: ACS-PRF grant no. 39427) and Oakland University, MI, USA, are acknowledged.

AUTHOR CONTRIBUTIONS

ABR-6 cages were synthesized by P.U.A.I.F., P.T.C., and B.D.B. PBR cages were synthesized by N.K.B. and K.R. Experiments were designed by S.K., P.U.A.I.F., J.M., A.S., and V.-V.T. Experiments were performed by S.K., P.U.A.I.F., J.M., A.S., R.K., and A.M.K. Modeling was planned and executed by P.L., J.M., and A.E. Manuscript was written by S.K., P.L., and V.-V.T. All authors were involved in discussion and analysis of the results as well as editing of the manuscript.

DECLARATION OF INTERESTS

The authors declare no competing interests.

Received: September 2, 2022
Revised: December 23, 2022
Accepted: January 18, 2023
Published: February 8, 2023

REFERENCES

1. Spence, M.M., Rubin, S.M., Dimitrov, I.E., Ruiz, E.J., Wemmer, D.E., Pines, A., Yao, S.Q., Tian, F., and Schultz, P.G. (2001). Functionalized xenon as a biosensor. Proc. Natl. Acad. Sci. USA *98*, 10654–10657. https://doi.org/10.1073/pnas.191368398.

2. Jayapaul, J., and Schröder, L. (2020). Molecular sensing with host systems for hyperpolarized ^{129}Xe. Molecules *25*, 4627. https://doi.org/10.3390/molecules25204627.

3. Wang, Y., and Dmochowski, I.J. (2016). An expanded palette of xenon-129 NMR biosensors. Acc. Chem. Res. *49*, 2179–2187. https://doi.org/10.1021/acs.accounts.6b00309.

4. Berthault, P., Huber, G., and Desvaux, H. (2009). Biosensing using laser-polarized xenon NMR/MRI. Prog. Nucl. Magn. Reson. Spectrosc. *55*, 35–60. https://doi.org/10.1016/j.pnmrs.2008.11.003.

5. Barskiy, D.A., Coffey, A.M., Nikolaou, P., Mikhaylov, D.M., Goodson, B.M., Branca, R.T., Lu, G.J., Shapiro, M.G., Telkki, V.-V., Zhivonitko, V.V., et al. (2017). NMR hyperpolarization techniques of gases. Chemistry *23*, 725–751. https://doi.org/10.1002/chem.201603884.

6. Schröder, L., Lowery, T.J., Hilty, C., Wemmer, D.E., and Pines, A. (2006). Molecular imaging using a targeted magnetic resonance hyperpolarized biosensor. Science *314*, 446–449. https://doi.org/10.1126/science.1131847.

7. Klippel, S., Döpfert, J., Jayapaul, J., Kunth, M., Rossella, F., Schnurr, M., Witte, C., Freund, C., and Schröder, L. (2014). Cell tracking with caged xenon: using cryptophanes as MRI reporters upon cellular internalization. Angew. Chem. Int. Ed. Engl. *53*, 493–496. https://doi.org/10.1002/anie.201307290.

8. Yang, S., Jiang, W., Ren, L., Yuan, Y., Zhang, B., Luo, Q., Guo, Q., Bouchard, L.-S., Liu, M., and Zhou, X. (2016). Biothiol xenon MRI sensor based on thiol-addition reaction. Anal. Chem. *88*, 5835–5840. https://doi.org/10.1021/acs.analchem.6b00403.

9. Hane, F.T., Li, T., Smylie, P., Pellizzari, R.M., Plata, J.A., DeBoef, B., and Albert, M.S. (2017). In vivo detection of cucurbit[6]uril, a hyperpolarized xenon contrast agent for a xenon magnetic resonance imaging biosensor. Sci. Rep. *7*, 41027. https://doi.org/10.1038/srep41027.

10. Wang, Y., and Dmochowski, I.J. (2015). Cucurbit[6]uril is an ultrasensitive ^{129}Xe NMR contrast agent. Chem. Commun. *51*, 8982–8985. https://doi.org/10.1039/C5CC01826A.

11. Döpfert, J., Schnurr, M., Kunth, M., Rose, H.M., Hennig, A., and Schröder, L. (2018). Time-resolved monitoring of enzyme activity with ultrafast Hyper-CEST spectroscopy. Magn. Reson. Chem. *56*, 679–688. https://doi.org/10.1002/mrc.4702.

12. Finbloom, J.A., Slack, C.C., Bruns, C.J., Jeong, K., Wemmer, D.E., Pines, A., and Francis, M.B. (2016). Rotaxane-mediated suppression and activation of cucurbit[6]uril for molecular detection by ^{129}Xe HyperCEST NMR. Chem. Commun. *52*, 3119–3122. https://doi.org/10.1039/C5CC10410F.

13. Adiri, T., Marciano, D., and Cohen, Y. (2013). Potential ^{129}Xe-NMR biosensors based on secondary and tertiary complexes of a water-soluble pillar[5]arene derivative. Chem. Commun. *49*, 7082–7084. https://doi.org/10.1039/C3CC43253J.

14. Fernando, P.U.A.I., Shepelytskyi, Y., Cesana, P.T., Wade, A., Grynko, V., Mendieta, A.M., Seveney, L.E., Brown, J.D., Hane, F.T., Albert, M.S., and DeBoef, B. (2020). Decacationic pillar[5]arene: a new scaffold for the development of ^{129}Xe MRI imaging agents. ACS Omega *5*, 27783–27788. https://doi.org/10.1021/acsomega.0c02565.

15. Robbins, T.A., Knobler, C.B., Bellew, D.R., and Cram, D.J. (1994). Host-guest complexion .67. A highly adaptive and strongly binding hemicarcerand. J. Am. Chem. Soc. *116*, 111–122. https://doi.org/10.1021/ja00080a014.

16. Roukala, J., Zhu, J., Giri, C., Rissanen, K., Lantto, P., and Telkki, V.-V. (2015). Encapsulation of xenon by a self-assembled Fe_4L_6 metallospramolecular cage. J. Am. Chem. Soc. *137*, 2464–2467. https://doi.org/10.1021/ja5130176.

17. Jayapaul, J., Komulainen, S., Zhivonitko, V.V., Mareš, J., Giri, C., Rissanen, K., Lantto, P., Telkki, V.V., and Schröder, L. (2022). Hyper-CEST NMR of metal organic polyhedral cages reveals hidden diastereomers with diverse guest exchange kinetics. Nat. Commun. *13*, 1708. https://doi.org/10.1038/s41467-022-29249-w.

18. Song, Y.-Q., Goodson, B.M., Taylor, R.E., Laws, D.D., Navon, G., and Pines, A. (1997). Selective enhancement of NMR signals for α-cyclodextrin with laser-polarized xenon. Angew. Chem. Int. Ed. Engl. *36*, 2368–2370. https://doi.org/10.1002/anie.199723681.

19. Hane, F.T., Fernando, A., Prete, B.R.J., Peloquin, B., Karas, S., Chaudhuri, S., Chahal, S., Shepelytskyi, Y., Wade, A., Li, T., et al. (2018). Cyclodextrin-based pseudorotaxanes: easily conjugatable scaffolds for synthesizing hyperpolarized xenon-129 magnetic resonance imaging agents. ACS Omega *3*, 677–681. https://doi.org/10.1021/acsomega.7b01744.

20. Fukutomi, J., Adachi, Y., Kaneko, A., Kimura, A., and Fujiwara, H. (2007). Inclusion complex formation of thiacalix[4]arene and Xe in aqueous solution studied by hyperpolarized ^{129}Xe NMR. J. Incl. Phenom. Macrocycl. Chem. *58*, 115–122. https://doi.org/10.1007/s10847-006-9130-1.

21. Nie, S.-X., Guo, H., Huang, T.-Y., Ao, Y.-F., Wang, D.-X., and Wang, Q.-Q. (2020). Xenon binding by a tight yet adaptive chiral soft capsule. Nat. Commun. *11*, 6257. https://doi.org/10.1038/s41467-020-20081-8.

22. Rose, H.M., Witte, C., Rossella, F., Klippel, S., Freund, C., and Schröder, L. (2014). Development of an antibody-based, modular biosensor for ^{129}Xe NMR molecular imaging of cells at nanomolar concentrations. Proc. Natl. Acad. Sci. USA *111*, 11697–11702. https://doi.org/10.1073/pnas.1406797111.

23. Stevens, T.K., Palaniappan, K.K., Ramirez, R.M., Francis, M.B., Wemmer, D.E., and Pines, A. (2013). HyperCEST detection of a ^{129}Xe-based contrast agent composed of cryptophane-A molecular cages on a bacteriophage scaffold. Magn. Reson. Med. *69*, 1245–1252. https://doi.org/10.1002/mrm.24371.

24. Palaniappan, K.K., Ramirez, R.M., Bajaj, V.S., Wemmer, D.E., Pines, A., and Francis, M.B. (2013). Molecular imaging of cancer cells using a bacteriophage-based ^{129}Xe NMR biosensor. Angew. Chem. Int. Ed. Engl. *52*, 4849–4853. https://doi.org/10.1002/anie.201300170.

25. Shapiro, M.G., Ramirez, R.M., Sperling, L.J., Sun, G., Sun, J., Pines, A., Schaffer, D.V., and Bajaj, V.S. (2014). Genetically encoded reporters for hyperpolarized xenon magnetic resonance imaging. Nat. Chem. *6*, 629–634. https://doi.org/10.1038/nchem.1934.

26. Stevens, T.K., Ramirez, R.M., and Pines, A. (2013). Nanoemulsion contrast agents with sub-picomolar sensitivity for xenon NMR. J. Am. Chem. Soc. *135*, 9576–9579. https://doi.org/10.1021/ja402885q.

27. Jeong, K., Netirojjanakul, C., Munch, H.K., Sun, J., Finbloom, J.A., Wemmer, D.E., Pines, A., and Francis, M.B. (2016). Targeted molecular imaging of cancer cells using MS2-based ^{129}Xe NMR. Bioconjug. Chem. *27*, 1796–1801. https://doi.org/10.1021/acs.bioconjchem.6b00275.

28. Klippel, S., Freund, C., and Schröder, L. (2014). Multichannel MRI labeling of mammalian cells by switchable nanocarriers for hyperpolarized xenon. Nano Lett. *14*, 5721–5726. https://doi.org/10.1021/nl502498w.

29. Wang, Y., Roose, B.W., Philbin, J.P., Doman, J.L., and Dmochowski, I.J. (2016). A genetically encoded β-lactamase reporter for ultrasensitive ^{129}Xe NMR in mammalian cells. Angew. Chem. Int. Ed. Engl. *55*, 8984–8987. https://doi.org/10.1002/anie.201604055.

30. Schnurr, M., Sydow, K., Rose, H.M., Dathe, M., and Schröder, L. (2015). Brain endothelial cell targeting via a peptide-functionalized liposomal carrier for xenon hyper-CEST MRI. Adv. Healthc. Mater. *4*, 40–45. https://doi.org/10.1002/adhm.201400224.

31. Schnurr, M., Volk, I., Nikolenko, H., Winkler, L., Dathe, M., and Schröder, L. (2020). Functionalized lipopeptide micelles as highly efficient NMR depolarization seed points for targeted cell labelling in xenon MRI. Adv. Biosyst. *4*, 1900251. https://doi.org/10.1002/adbi.201900251.

32. Meldrum, T., Schröder, L., Denger, P., Wemmer, D.E., and Pines, A. (2010). Xenon-based molecular sensors in lipid suspensions. J. Magn. Reson. *205*, 242–246. https://doi.org/10.1016/j.jmr.2010.05.005.

33. Ullah, M.S., Zhivonitko, V.V., Samoylenko, A., Zhyvolozhnyi, A., Viitala, S., Kankaanpää, S., Komulainen, S., Schröder, L., Vainio, S.J., and Telkki, V.-V. (2021). Identification of

extracellular nanoparticle subsets by nuclear magnetic resonance. Chem. Sci. *12*, 8311–8319. https://doi.org/10.1039/D1SC01402A.

34. Hoegberg, A.G.S. (1980). Two stereoisomeric macrocyclic resorcinol-acetaldehyde condensation products. J. Org. Chem. *45*, 4498–4500. https://doi.org/10.1021/jo01310a046.

35. Beyeh, N.K., Valkonen, A., and Rissanen, K. (2010). Piperazine bridged resorcinarene cages. Org. Lett. *12*, 1392–1395. https://doi.org/10.1021/ol100407f.

36. Sears, D.N., and Jameson, C.J. (2003). Theoretical calculations of the Xe chemical shifts in cryptophane cages. J. Chem. Phys. *119*, 12231–12244. https://doi.org/10.1063/1.1625364.

37. Bagno, A., and Saielli, G. (2012). Understanding the extraordinary deshielding of ^{129}Xe in a permetallated cryptophane by relativistic DFT. Chemistry *18*, 7341–7345. https://doi.org/10.1002/chem.201103979.

38. Straka, M., Lantto, P., and Vaara, J. (2008). Toward calculations of the ^{129}Xe chemical shift in Xe@C60 at experimental conditions: relativity, correlation, and dynamics. J. Phys. Chem. A *112*, 2658–2668. https://doi.org/10.1021/jp711674y.

39. Standara, S., Kulhánek, P., Marek, R., Horníček, J., Bouř, P., and Straka, M. (2011). Simulations of ^{129}Xe NMR chemical shift of atomic xenon dissolved in liquid benzene. Theor. Chem. Acc. *129*, 677–684. https://doi.org/10.1007/s00214-011-0930-z.

40. Standara, S., Kulhánek, P., Marek, R., and Straka, M. (2013). ^{129}Xe NMR chemical shift in Xe@C60 calculated at experimental conditions: essential role of the relativity, dynamics, and explicit solvent. J. Comput. Chem. *34*, 1890–1898. https://doi.org/10.1002/jcc.23334.

41. Selent, M., Nyman, J., Roukala, J., Ilczyszyn, M., Oilunkaniemi, R., Bygrave, P.J., Laitinen, R., Jokisaari, J., Day, G.M., and Lantto, P. (2017). Clathrate structure determination by combining crystal structure prediction with computational and experimental ^{129}Xe NMR spectroscopy. Chemistry *23*, 5258–5269. https://doi.org/10.1002/chem.201604797.

42. Jameson, C.J., Jameson, A.K., Baello, B.I., and Lim, H. (1994). Grand canonical Monte Carlo simulations of the distribution and chemical shifts of xenon in the cages of zeolite NaA. I. distribution and ^{129}Xe chemical shifts. J. Chem. Phys. *100*, 5965–5976. https://doi.org/10.1063/1.467108.

43. Kantola, J.-H., Vaara, J., Rantala, T.T., and Jokisaari, J. (1997). Xe^{129} adsorbed in AlPO4-11 molecular sieve: molecular dynamics simulation of adsorbate dynamics and NMR chemical shift. J. Chem. Phys. *107*, 6470–6478. https://doi.org/10.1063/1.475135.

44. Trepte, K., Schaber, J., Schwalbe, S., Drache, F., Senkovska, I., Kaskel, S., Kortus, J., Brunner, E., and Seifert, G. (2017). The origin of the measured chemical shift of ^{129}Xe in UiO-66 and UiO-67 revealed by DFT investigations. Phys. Chem. Chem. Phys. *19*, 10020–10027. https://doi.org/10.1039/C7CP00852J.

45. Kemnitzer, T.W., Tschense, C.B.L., Wittmann, T., Rössler, E.A., and Senker, J. (2018). Exploring local disorder within CAU-1 frameworks using hyperpolarized ^{129}Xe NMR spectroscopy. Langmuir *34*, 12538–12548. https://doi.org/10.1021/acs.langmuir.8b02592.

46. Komulainen, S., Roukala, J., Zhivonitko, V.V., Javed, M.A., Chen, L., Holden, D., Hasell, T., Cooper, A., Lantto, P., and Telkki, V.-V. (2017). Inside information on xenon adsorption in porous organic cages by NMR. Chem. Sci. *8*, 5721–5727. https://doi.org/10.1039/C7SC01990D.

47. Håkansson, P., Javed, M.A., Komulainen, S., Chen, L., Holden, D., Hasell, T., Cooper, A., Lantto, P., and Telkki, V.-V. (2019). NMR relaxation and modelling study of the dynamics of SF_6 and Xe in porous organic cages. Phys. Chem. Chem. Phys. *21*, 24373–24382. https://doi.org/10.1039/C9CP04379A.

48. Karjalainen, J., Vaara, J., Straka, M., and Lantto, P. (2015). Xenon NMR of liquid crystals confined to cylindrical nanocavities: a simulation study. Phys. Chem. Chem. Phys. *17*, 7158–7171. https://doi.org/10.1039/C4CP04868G.

49. Peuravaara, P., Karjalainen, J., Zhu, J., Mareš, J., Lantto, P., and Vaara, J. (2018). Chemical shift extremum of ^{129}Xe(aq) reveals details of hydrophobic solvation. Sci. Rep. *8*, 7023. https://doi.org/10.1038/s41598-018-25418-4.

50. Mecozzi, S., and Rebek Jr, J. (1998). The 55% solution: a formula for molecular recognition in the liquid state. Chem. Eur J. *4*, 1016–1022. https://doi.org/10.1002/(SICI)1521-3765(19980615)4:6<1016::AID-CHEM1016>3.0.CO;2-B.

51. CAVER Analyst 2.0, Analysis and Visualization of Tunnels and Chan-Nels in Biomolecules Home Page. http://www.caver.cz/.

52. Taratula, O., Hill, P.A., Khan, N.S., Carroll, P.J., and Dmochowski, I.J. (2010). Crystallographic observation of 'induced fit' in a cryptophane host–guest model system. Nat. Commun. *1*, 148. https://doi.org/10.1038/ncomms1151.

53. Fogarty, H.A., Berthault, P., Brotin, T., Huber, G., Desvaux, H., and Dutasta, J.-P. (2007). A cryptophane core optimized for xenon encapsulation. J. Am. Chem. Soc. *129*, 10332–10333. https://doi.org/10.1021/ja073771c.

54. Mills, G., Jónsson, H., and Schenter, G.K. (1995). Reversible work transition state theory: application to dissociative adsorption of hydrogen. Surf. Sci. *324*, 305–337. https://doi.org/10.1016/0039-6028(94)00731-4.

55. Ásgeirsson, V., Birgisson, B.O., Bjornsson, R., Becker, U., Neese, F., Riplinger, C., and Jónsson, H. (2021). Nudged elastic band method for molecular reactions using energy-weighted springs combined with eigenvector following. J. Chem. Theory Comput. *17*, 4929–4945. https://doi.org/10.1021/acs.jctc.1c00462.

56. Fairchild, R.M., Joseph, A.I., Holman, K.T., Fogarty, H.A., Brotin, T., Dutasta, J.P., Boutin, C., Huber, G., and Berthault, P. (2010). A water-soluble Xe@cryptophane-111 complex exhibits very high thermodynamic stability and a peculiar ^{129}Xe NMR chemical shift. J. Am. Chem. Soc. *132*, 15505–15507. https://doi.org/10.1021/ja1071515.

57. Weiland, E., Springuel-Huet, M.-A., Nossov, A., and Gédéon, A. (2016). ^{129}Xenon NMR: review of recent insights into porous materials. Microporous Mesoporous Mater. *225*, 41–65. https://doi.org/10.1016/j.micromeso.2015.11.025.

58. Hanni, M., Lantto, P., and Vaara, J. (2009). Pairwise additivity in the nuclear magnetic resonance interactions of atomic xenon. Phys. Chem. Chem. Phys. *11*, 2485–2496. https://doi.org/10.1039/B821907A.

59. Bo, S., Battino, R., and Wilhelm, E. (1993). Solubility of gases in liquids. 19. solubility of He, Ne, Ar, Kr, Xe, N_2, O_2, CH_4, CF_4, and SF_6 in normal 1-alkanols n-$C_lH_{2l+1}OH$ ($1 \leq l \leq 11$) at 298.15 K. J. Chem. Eng. Data *38*, 611–616. https://doi.org/10.1021/je00012a035.

60. Kunth, M., Witte, C., and Schröder, L. (2015). Continuous-wave saturation considerations for efficient xenon depolarization. NMR Biomed. *28*, 601–606. https://doi.org/10.1002/nbm.3307.

61. Huber, G., Beguin, L., Desvaux, H., Brotin, T., Fogarty, H.A., Dutasta, J.-P., and Berthault, P. (2008). Cryptophane-xenon complexes in organic solvents observed through NMR spectroscopy. J. Phys. Chem. A *112*, 11363–11372. https://doi.org/10.1021/jp807425t.

62. Bartik, K., Luhmer, M., Dutasta, J.-P., Collet, A., and Reisse, J. (1998). ^{129}Xe and ^{1}H NMR study of the reversible trapping of xenon by cryptophane-A in organic solution. J. Am. Chem. Soc. *120*, 784–791. https://doi.org/10.1021/ja972377j.

63. Hill, P.A., Wei, Q., Eckenhoff, R.G., and Dmochowski, I.J. (2007). Thermodynamics of xenon binding to cryptophane in water and human plasma. J. Am. Chem. Soc. *129*, 9262–9263. https://doi.org/10.1021/ja072965p.

64. Jacobson, D.R., Khan, N.S., Collé, R., Fitzgerald, R., Laureano-Pérez, L., Bai, Y., and Dmochowski, I.J. (2011). Measurement of radon and xenon binding to a cryptophane molecular host. Proc. Natl. Acad. Sci. USA *108*, 10969–10973. https://doi.org/10.1073/pnas.1105227108.

65. Bartik, K., Luhmer, M., Heyes, S.J., Ottinger, R., and Reisse, J. (1995). Probing molecular cavities in alpha-cyclodextrin solutions by xenon NMR. J. Magn. Reson. B *109*, 164–168. https://doi.org/10.1006/jmrb.1995.0005.

66. Keeler, J. (2010). Understanding NMR Spectroscopy, 2nd Ed. (John Wiley & Sons).

67. Swift, T.J., and Connick, R.E. (1962). NMR-relaxation mechanisms of O^{17} in aqueous solutions of paramagnetic cations and the lifetime of water molecules in the first coordination sphere. J. Chem. Phys. *37*, 307–320. https://doi.org/10.1063/1.1701321.

68. Kunth, M., and Schröder, L. (2020). Binding site exchange kinetics revealed through efficient spin–spin dephasing of hyperpolarized ^{129}Xe. Chem. Sci. *12*, 158–169. https://doi.org/10.1039/D0SC04835F.

69. Gomes, M.D., Dao, P., Jeong, K., Slack, C.C., Vassiliou, C.C., Finbloom, J.A., Francis, M.B., Wemmer, D.E., and Pines, A. (2016). ^{129}Xe

NMR relaxation-based macromolecular sensing. J. Am. Chem. Soc. *138*, 9747–9750. https://doi.org/10.1021/jacs.6b02758.

70. Beyeh, N.K., Díez, I., Taimoory, S.M., Meister, D., Feig, A.I., Trant, J.F., Ras, R.H.A., and Rissanen, K. (2018). High-affinity and selective detection of pyrophosphate in water by a resorcinarene salt receptor. Chem. Sci. *9*, 1358–1367. https://doi.org/10.1039/C7SC05167K.

71. Kazakova, E.K., Makarova, N.A., Ziganshina, A.U., Muslinkina, L.A., Muslinkin, A.A., and Habicher, W.D. (2000). Novel water-soluble tetrasulfonatomethylcalix[4]resorcinarenes. Tetrahedron Lett. *41*, 10111–10115. https://doi.org/10.1016/S0040-4039(00)01798-6.

72. Twum, K., Rautiainen, J.M., Yu, S., Truong, K.-N., Feder, J., Rissanen, K., Puttreddy, R., and Beyeh, N.K. (2020). Host–guest interactions of sodiumsulfonatomethyleneresorcinarene and quaternary ammonium halides: an experimental–computational analysis of the guest inclusion properties. Cryst. Growth Des. *20*, 2367–2376. https://doi.org/10.1021/acs.cgd.9b01540.

73. Ratcliffe, C.I. (1998). Xenon Nmr. Annu. Rep. NMR Spectrosc. *36*, 123–221. https://doi.org/10.1016/S0066-4103(08)60007-1.

74. McHugh, C.T., Kelley, M., Bryden, N.J., and Branca, R.T. (2022). In vivo hyperCEST imaging: experimental considerations for a reliable contrast. Magn. Reson. Med. *87*, 1480–1489. https://doi.org/10.1002/mrm.29032.

75. Shimoyama, D., Ikeda, T., Sekiya, R., and Haino, T. (2017). Synthesis and structure of feet-to-feet connected bisresorcinarenes. J. Org. Chem. *82*, 13220–13230. https://doi.org/10.1021/acs.joc.7b02301.

76. Murase, K., and Tanki, N. (2011). Numerical solutions to the time-dependent Bloch equations revisited. Magn. Reson. Imaging *29*, 126–131. https://doi.org/10.1016/j.mri.2010.07.003.

77. McConnell, H.M. (1958). Reaction rates by nuclear magnetic resonance. J. Chem. Phys. *28*, 430–431. https://doi.org/10.1063/1.1744152.

78. Simulation of CEST MRI Data Home Page. https://github.com/JCardenasRdz/CESTMRI.mat.

79. Linden, W.V.D., Preuss, R., and Dose, V. (1998). The prior-predictive value: a paradigm of nasty multi-dimensional integrals. In Maximum Entropy and Bayesian Methods, W.V.D. Linden, V. Dose, R. Fischer, and R. Preuss, eds. (Netherlands: Kluwer Academic Publishers, Springer), pp. 319–326.

80. Håkansson, P. (2021). Relaxometry models compared with Bayesian techniques: ganglioside micelle Example. Phys. Chem. Chem. Phys. *23*, 2637–2648. https://doi.org/10.1039/D0CP04750C.

81. Balasubramani, S.G., Chen, G.P., Coriani, S., Diedenhofen, M., Frank, M.S., Franzke, Y.J., Furche, F., Grotjahn, R., Harding, M.E., Hättig, C., et al. (2020). TURBOMOLE: modular program suite for ab initio quantum-chemical and condensed-matter simulations. J. Chem. Phys. *152*, 184107. https://doi.org/10.1063/5.0004635.

82. TURBOMOLE V7.5 (2020). Program Package for Electronic Structure Calculations Home Page. https://www.turbomole.org.

83. Adamo, C., and Barone, V. (1999). Toward reliable density functional methods without adjustable parameters: the PBE0 model. J. Chem. Phys. *110*, 6158–6170. https://doi.org/10.1063/1.478522.

84. Caldeweyher, E., Ehlert, S., Hansen, A., Neugebauer, H., Spicher, S., Bannwarth, C., and Grimme, S. (2019). A generally applicable atomic-charge dependent London dispersion correction. J. Chem. Phys. *150*, 154122. https://doi.org/10.1063/1.5090222.

85. Franzke, Y.J., Middendorf, N., and Weigend, F. (2018). Efficient implementation of one- and two-component analytical energy gradients in exact two-component theory. J. Chem. Phys. *148*, 104110. https://doi.org/10.1063/1.5022153.

86. Franzke, Y.J., Treß, R., Pazdera, T.M., and Weigend, F. (2019). Error-consistent segmented contracted all- electron relativistic basis sets of double- and triple-zeta quality for NMR shielding constants. Phys. Chem. Chem. Phys. *21*, 16658–16664. https://doi.org/10.1039/C9CP02382H.

87. Weigend, F., and Ahlrichs, R. (2005). Balanced basis sets of split valence, triple zeta valence and quadruple zeta valence quality for H to Rn: design and assessment of accuracy. Phys. Chem. Chem. Phys. *7*, 3297–3305. https://doi.org/10.1039/B508541A.

88. Klamt, A., and Schüürmann, G. (1993). COSMO: a new approach to dielectric screening in solvents with explicit expressions for the screening energy and its gradient. J. Chem. Soc. Perkin Trans. *2*, 799–805. https://doi.org/10.1039/P29930000799.

89. Perdew, J.P., Burke, K., and Ernzerhof, M. (1996). Generalized gradient approximation made simple. Phys. Rev. Lett. *77*, 3865–3868. https://doi.org/10.1103/PhysRevLett.77.3865.

90. Lee, C., Yang, W., and Parr, R.G. (1988). Development of the Colle-Salvetti correlation-energy formula into a functional of the electron density. Phys. Rev. B Condens. Matter *37*, 785–789. https://doi.org/10.1103/PhysRevB.37.785.

91. Becke, A.D. (1993). Density-functional thermochemistry. III. The role of exact exchange. J. Chem. Phys. *98*, 5648–5652. https://doi.org/10.1063/1.464913.

92. Schreckenbach, G., and Ziegler, T. (1995). Calculation of NMR shielding tensors using gauge-including atomic orbitals and modern density functional theory. J. Phys. Chem. *99*, 606–611. https://doi.org/10.1021/j100002a024.

93. Wolff, S.K., Ziegler, T., van Lenthe, E., and Baerends, E.J. (1999). Density functional calculations of nuclear magnetic shieldings using the zeroth-order regular approximation (ZORA) for relativistic effects: ZORA nuclear magnetic resonance. J. Chem. Phys. *110*, 7689–7698. https://doi.org/10.1063/1.478680.

94. te Velde, G., Bickelhaupt, F.M., Baerends, E.J., Fonseca Guerra, C., van Gisbergen, S.J.A., Snijders, J.G., and Ziegler, T. (2001). Chemistry with ADF. J. Comput. Chem. *22*, 931–967. https://doi.org/10.1002/jcc.1056.

95. ADF (2020). SCM, Software for Chemistry & Materials Home Page. http://www.scm.com.

96. Van Lenthe, E., and Baerends, E.J. (2003). Optimized slater-type basis sets for the elements 1–118. J. Comput. Chem. *24*, 1142–1156. https://doi.org/10.1002/jcc.10255.

97. Autschbach, J. (2009). Magnitude of finite-nucleus-size effects in relativistic density functional computations of indirect NMR nuclear spin-spin coupling constants. Chemphyschem *10*, 2274–2283. https://doi.org/10.1002/cphc.200900271.

98. Franzke, Y.J., and Weigend, F. (2019). NMR shielding tensors and chemical shifts in scalar-relativistic local exact two-component theory. J. Chem. Theory Comput. *15*, 1028–1043. https://doi.org/10.1021/acs.jctc.8b01084.

99. Bannwarth, C., Caldeweyher, E., Ehlert, S., Hansen, A., Pracht, P., Seibert, J., Spicher, S., and Grimme, S. (2021). Extended tight-binding quantum chemistry methods. WIREs Comput. Mol. Sci. *11*, e0149. https://doi.org/10.1002/wcms.1493.

100. Grimme, S., Bannwarth, C., and Shushkov, P. (2017). A robust and accurate tight-binding quantum chemical method for structures, vibrational frequencies, and noncovalent interactions of large molecular systems parametrized for all spd-block elements (Z = 1–86). J. Chem. Theory Comput. *13*, 1989–2009. https://doi.org/10.1021/acs.jctc.7b00118.

101. Bannwarth, C., Ehlert, S., and Grimme, S. (2019). GFN2-xTB—an accurate and broadly parametrized self-consistent tight-binding quantum chemical method with multipole electrostatics and density-dependent dispersion contributions. J. Chem. Theory Comput. *15*, 1652–1671. https://doi.org/10.1021/acs.jctc.8b01176.

102. Brandenburg, J.G., Bannwarth, C., Hansen, A., and Grimme, S. (2018). B97-3c: a revised low-cost variant of the B97-D density functional method. J. Chem. Phys. *148*, 064104. https://doi.org/10.1063/1.5012601.

103. Ehlert, S., Stahn, M., Spicher, S., and Grimme, S. (2021). Robust and efficient implicit solvation model for fast semiempirical methods. J. Chem. Theory Comput. *17*, 4250–4261. https://doi.org/10.1021/acs.jctc.1c00471.

104. Marenich, A.V., Cramer, C.J., and Truhlar, D.G. (2009). Universal solvation model based on solute electron density and on a continuum model of the solvent defined by the bulk dielectric constant and atomic surface tensions. J. Phys. Chem. B *113*, 6378–6396. https://doi.org/10.1021/jp810292n.